Journal of Materials Chemistry C

Understanding the effect of light and temperature on the optical properties and stability of mixed-ion halide perovskites

Journal:	*Journal of Materials Chemistry C*
Manuscript ID	TC-ART-04-2020-002103.R1
Article Type:	Paper
Date Submitted by the Author:	11-Jun-2020
Complete List of Authors:	Wieghold, Sarah; Florida State University, Chemistry and Biochemistry Bieber, Alexander; Florida State University, Chemistry and Biochemistry Mardani, Masoud; National High Magnetic Field Laboratory Siegrist, Theo; FAMU-FSU College of Engineering; National High Magnetic Field Laboratory, Nienhaus, Lea; Florida State University, Chemistry and Biochemistry

Understanding the effect of light and temperature on the optical properties and stability of mixed-ion halide perovskites

Sarah Wieghold,[1,#,] Alexander S. Bieber,[1] Masoud Mardani,[2] Theo Siegrist,[2,3] Lea Nienhaus[1,*]*

[1]Department of Chemistry and Biochemistry, Florida State University, Tallahassee, FL 32306, USA

[2]National High Magnetic Field Laboratory, Florida State University, Tallahassee, FL 32310 USA

[3]FAMU-FSU College of Engineering, Tallahassee, FL 32310

*corresponding Author: swieghold@fsu.edu and lnienhaus@fsu.edu

ABSTRACT

The stability of organic-inorganic halide perovskite films plays an important role for their successful incorporation as absorber materials in solar cells under realistic operation conditions. While light-induced effects have been observed and traced to phase segregation, the impact of different stressors simultaneously is mostly unexplored. In this work, we investigate the combined influence of light and elevated temperature on the performance of mixed-cation mixed-halide perovskites. In particular, we compare the effect of different A-site cations on the photoluminescence (PL) properties and film stability when both stressors are used simultaneously. We find two pathways underlying the PL peak reduction and PL shift in the optical properties. For perovskite films composed of formamidinium and methylammonium as A-site cations, we can correlate the decrease in film performance to the formation of $Pb(I,Br)_2$ and an increase in electron-phonon interactions. Similarly, Rb doping in the perovskite film exhibits comparable results. Contrary, using Cs as an additional A-site cation greatly enhances the overall performance and results in more stable film structures which indicates that Cs is effective in stiffening the perovskite lattice, which can be attributed to a better size match for the $Pb(I,Br)_3$ sublattice as predicted by the Goldschmidt tolerance factor. These findings suggest that it is of importance to carefully select stressors when assessing performance related parameters of perovskite solar cells.

Introduction

Hybrid metal halide perovskites have been extensively studied over the last decade due to their promising material properties such as long carrier lifetimes and minority carrier diffusion lengths, tunable bandgap, as well as the desired high absorption cross sections throughout the visible and near infrared spectrum.[1–9] Despite being a promising absorber material for applications in photovoltaics (PVs) or emitter in light emitting diodes (LEDs), it was soon recognized that hybrid metal halide perovskites suffer from instability issues caused by degradation processes and phase transitions at elevated temperatures.[9–11] To mitigate these initial drawbacks, mixed-ion double perovskites or lower dimensional perovskite-related materials were developed which exhibit an improved stability at elevated temperatures relevant to PV applications.[12–16] In particular, the incorporation of additional cations which fit into the Goldschmidt tolerance factor for stable perovskite structures or a substitution of the B-site compound resulted in an enhanced stability with record PV efficiencies.[12,13,17–21]

However, when compared to established PV materials, perovskite-based materials still lack long-term stability and show a decrease in performance over time. To unravel the underlying root causes, the effect of stressors on the perovskite performance have been widely studied,[22,23] for example moisture or oxygen,[24,25] or thermal and photoinduced effects.[26–32]

Recently, it was proposed to establish “International Summit on Organic PV Stability” (ISOS) protocols which can be used on a lab scale to compare stability and performance related parameters of perovskite solar cells.[33] For example to assess device stabilities, the ISOS-D-2 protocol can be used to study the effect of temperature on the performance at elevated temperatures of 65 or 85 °C. It is worth drawing parallels to the silicon community here: silicon solar modules are tested via International Electrotechnical Commission (IEC) standards, e.g. IEC 61215, and it was recognized later that by using two stressors simultaneously, new degradation mechanisms emerge. For example, in multicrystalline silicon passivated emitter

and rear cells a phenomenon called light- and elevated temperature-induced degradation (LeTID) was discovered in modules already installed in the field. LeTID has a severe impact on the relative degradation rate of PV modules.[34–36]

In this work, we study the combined effect of light and elevated temperature on the stability of mixed-ion perovskite thin films composed of $(FA_{0.83}MA_{0.17})Pb(I_{0.83}Br_{0.17})_3$. Because it has been shown that the choice of the A-site cation has the largest influence on the overall stability, we investigate different cations, Rb, Cs, and a mixture thereof, to assess the importance of the Goldschmidt tolerance factor toward structural stability and susceptibility.[37] To monitor the change in the optoelectronic properties of the films under the exposure of light and temperature, we use steady-state photoluminescence (PL) and (wavelength-dependent) time-correlated single photon counting (TCSPC) measurements. To compare these changes to structural variations in the underlying perovskite films, we employ X-ray diffraction (XRD) under combined light and elevated temperature exposure. We find a strong correlation between the structural stability of the films doped with either Cs, or Cs and Rb, and their optoelectronic properties. We also show that the underlying changes are only observable when both stressors, light and temperature, are used simultaneously. These findings suggest that it is of importance to carefully select the stressors when assessing performance related parameters of PSCs.

Results

For this study we fabricate four different films with varying multi-cation compositions to investigate the effect of the Goldschmidt tolerance factor on the mixed perovskite film stability under ambient conditions using two stressors simultaneously: light and elevated temperatures. The Goldschmidt tolerance factor *t* is an empirical index to assess film stability and distortion. It is commonly used as a measure for the maximum and minimum dimensions of the A-site cations suitable to form a stable halide perovskite lattice.[37,38] The tolerance factor *t* is defined

as the ratio of the ionic radii of the cations r_A and r_B, and the anion r_X: $t = (r_A+r_B)/(\sqrt{2}(r_B+r_X)$. For $0.8 < t < 1$, the desired photoactive black phase of the perovskite is obtained. We fabricate a control sample composed of $(FA_{0.83}MA_{0.17})Pb(I_{0.83}Br_{0.17})_3$ and we dope the following cations into the film at a 5% load: Rb, Cs, and both Rb and Cs.[13,39] It is well established that a stable photoactive cubic perovskite phase is formed for the cations MA and FA ($MAPbI_3$: t = 0.91, $FAPbI_3$: t = 0.99).[40] Cs falls within the Goldschmidt tolerance factor ($CsPbI_3$: $t = 0.81$) and can further stabilize the photoactive black phase, while Rb is seemingly too small to be incorporated into the perovskite lattice ($RbPbI_3$: $t = 0.77$).[12,13,24,37,41] However, we have recently shown that the addition of RbI results in a modification of the crystal lattice and can suppress the formation of the undesired PbI_2 phase resulting in enhanced film stability despite small Rb precipitations on the surface.[39,42] All films are prepared with an excess of PbI_2 and $PbBr_2$ (also referred to as 'overstoichiometric') which has been shown to increase PL decay lifetimes and extracted interfacial photocurrents.[39,43] The not encapsulated samples are labeled I/Br, Rb-I/Br, Cs-I/Br, and RbCs-I/Br for the bare undoped FAMA film and the additional cations Cs, Rb, and (Rb, Cs), respectively. All measurements were performed in ambient conditions under approx. 20% humidity.

The films are first characterized by optical spectroscopy at room temperature. Figure 1a-b show the optical characterization of the pristine samples which is in accordance with previous results.[42,44–46] Compare Figure S1 for absorbance spectra. In particular, all four samples exhibit an emission peak at ~790 nm under steady-state conditions at room temperature. We note, that under initial illumination the emission peak red-shifts within the first 180 s which can be attributed to halide segregation[27–29,47] (compare Figure S2 in the Supporting Information). To measure the PL decay dynamics of each sample, we perform time-correlated single photon counting (TCSPC) measurements (Figure 1b). The samples were first illuminated for 180 s prior to the measurement to account for the fast halide segregation. We find an initial fast decay

for all samples which can be attributed to a combination of rapid non-radiative recombination via trap states, band-to-band recombination, and hot carrier cooling[48] followed by a long-lived tail. The XRD pattern for all four films at room temperature are shown in Figure 1c confirming the cubic phase for all four samples (compare Supporting Information). AFM topography images of the pristine samples can be found in Figure S3 in the Supporting Information.

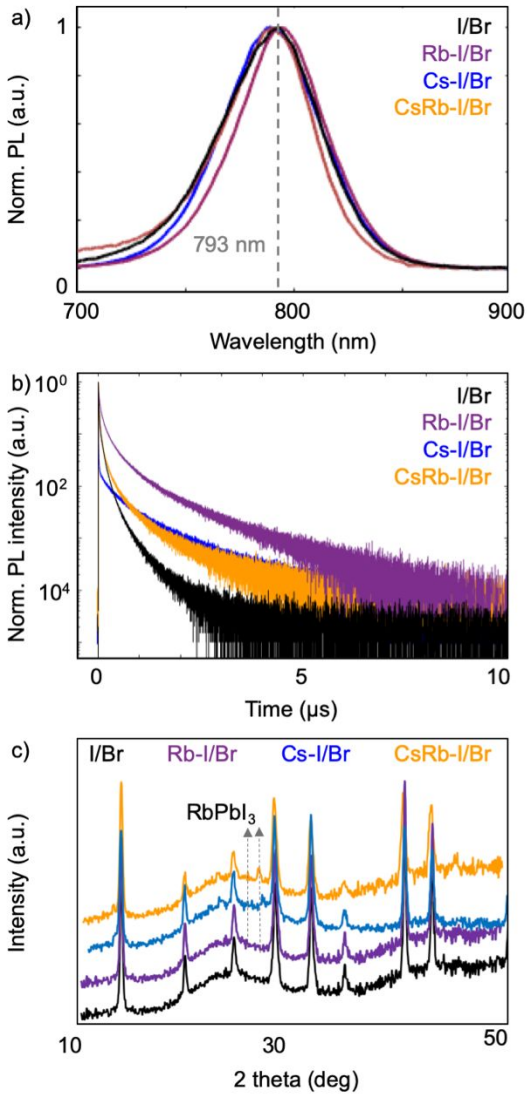

Figure 1. Optical and structural characterization of the pristine I/Br perovskite films doped with Cs, Rb or a mixture thereof at room temperature. a) steady-state PL spectra under 405 nm excitation. b) Time-resolved PL spectra showing the increased lifetime by adding Cs, Rb, and RbCs into the perovskite sample under pulsed 405 nm excitation (excitation density ~4 x 10^{16} cm^{-3}). c) XRD measurements of all four film compositions. The spectra are offset for clarification.

To gain more insight into the performance of the four films when multiple different stressors are applied simultaneously, e.g. light exposure and elevated temperatures, we perform steady-

state PL experiments at 85 °C under continuous-wave excitation at 405 nm at a laser power of 5 W/cm^2. Here, the samples are placed on a ceramic heater plate and mounted in the PL setup. The samples are first equilibrated at 25 °C for 2 min to ensure a consistent starting temperature for all films. Afterwards, the samples are heated to 85 °C with a temperature ramp of 2.3 ºC/min followed by a constant temperature hold at 85 °C for 20 min. The PL intensity is recorded as a function of time during the temperature ramp and at the constant temperature of 85 °C. The inset in Figure 2a shows the temperature profile used in this study. We find that all four samples exhibit an initial red-shift of the PL, an increase in the PL intensity, and a broadening of the PL peak (Figure 2a-h). After approx. 3.5 min, which corresponds to a temperature of ~33 °C, the PL starts to blue-shift accompanied with a decrease in the PL intensity for the I/Br and Rb-I/Br samples, whereas for the Cs-I/Br and RbCs-I/Br samples, the shift starts at around 5 min into the experiment corresponding to a slightly higher temperature of ~37 °C (Figure 2e-h). Additionally, the PL intensity decreases independent of the film composition when the samples are further heated to 85 °C. All films have a weak, yet detectable PL when the target temperature is reached at 85 °C. Interestingly, we find that during the temperature ramp, the PL intensity first decreases and then increases again when the films are doped with the cations compared to our standard film I/Br. This behavior is most pronounced in the Cs-I/Br film.

To decouple the influence of the different stressors, we perform the same steady-state experiments without applying our temperature profile, compare Figure S4. To conclude that light and temperature are both requisite for the underlying change in the PL, we also heated the samples first followed by PL measurements (Figure S5). For both experiments we find the same initial red-shift of the PL, a peak broadening and an increase in the PL intensity for all four samples compared to the experiment with light and temperature. However, no blue-shift or decrease in the PL is observed for longer times which hints that both stressors are needed simultaneously to explain the observed behavior. Additionally, we performed experiments

were the films were subjected to heat and illumination and stored overnight in the dark (Figure S6). We observe that the films recovered in the dark and the PL peak position shift is reversible.

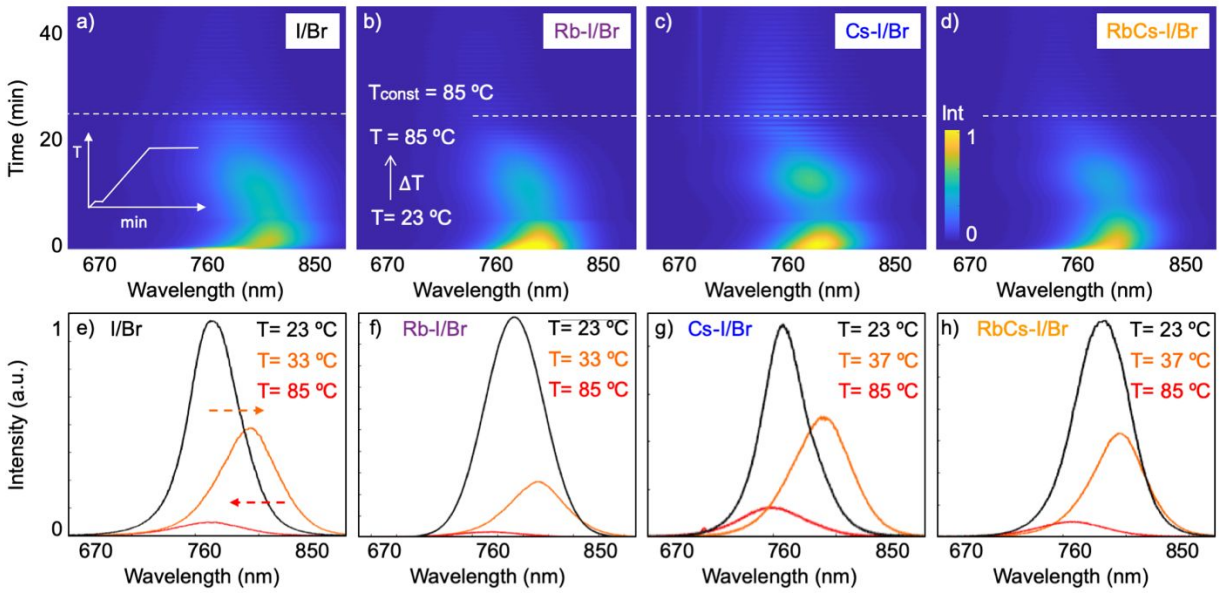

Figure 2. Steady-state PL under elevated temperatures. Waterfall plots of the different doped perovskite films for the a) bare I/Br, b) Rb-I/Br, c) Cs-I/Br, and RbCs-I/Br films. The temperature profile is shown as inset in a). The samples are first heated to 25 °C for 2 min to ensure the same starting conditions. The samples are then heated to 85 °C with a ramp of 2.3 °C/min followed by a constant temperature at 85 °C for 20 min. The PL spectra are taken every 2 s for a total time of 45 min. A continuous 405 nm laser with an incident power of 600 μW (~5 W/cm²) was used. The dashed lines in the images indicates the temperature of 85 °C. The intensity gradient is shown from a low PL intensity (blue) to a high PL intensity (yellow). e)-h) Extracted line profiles of the PL map at a temperature of 23 °C (black), a temperature of 33 °C for I/Br and Rb-I/Br and 37 °C for Cs-I/Br and RbCs-I/Br (yellow), and at the target temperature of 85 °C (red).

To further investigate this behavior and the observed shift in the PL peak, as well as the variation in the PL intensity under light and elevated temperatures, we turn to wavelength-dependent TCSPC experiments. In this measurement, the TCSPC setup is coupled to an interferometer consisting of two polarizers and two birefringent optical elements which allow to obtain a spectrum as a function of the optical frequency. Figure 3a-d show the obtained maps where we first record maps at room temperature for the pristine films (left column). The inset on the right side of each map shows the integrated counts of photons at each wavelength. Since this measurement can be considered as a slow, averaged measurement, we illuminate the

samples for 10 min prior to the measurement thus, we do not expect to see any influence caused by the initial red-shift in the PL peak.

The peak slightly blue-shifts for the I/Br, Cs-I/Br, and Rb-I/Br films, whereas no shift is observed for the RbCs-I/Br film (middle column) during the heating process of the samples. Upon reaching the target temperature of 85 °C, the peaks blue-shift significantly by 26 to 40 nm, where the smallest shift is seen for the RbCs-I/Br sample (right column). Since this measurement allows for wavelength-dependent lifetimes, we extract the decay dynamics for each map at the intensity peak and plot them in Figure 3e-h. For the I/Br sample (Figure 3e), we find that the lifetime decreases during the temperature ramp, and further decreases when the temperature reaches 85 °C. Contrary, an initial slight increase in the lifetime can be observed for the Rb-I/Br and Cs-I/Br samples (Figures 3f,g) during the heating process, followed by a decrease in lifetime when the sample temperature hits 85 °C. For the RbCs-I/Br sample shown in Figure 3h, we find the largest increase in lifetime by a factor of approximately 3x during the heating process. However, the lifetime drastically decreases when the sample temperature reaches the target temperature of 85 °C.

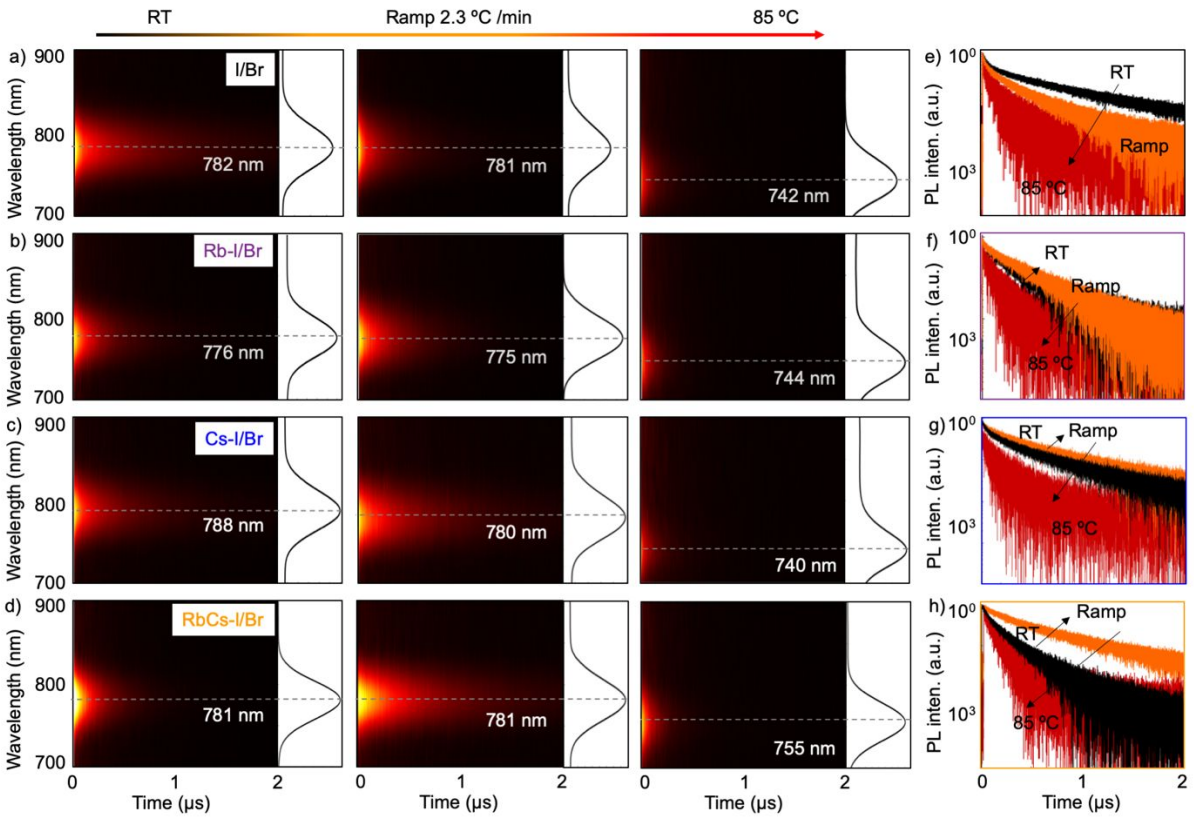

Figure 3. Wavelength-dependent lifetimes experiments for the a) I/Br, b) Rb-I/Br, c) Cs-I/Br, and d) RbCs-I/Br films. The left column shows the initial maps without temperature. The middle column is recorded during the temperature ramp, and the right column shows the maps when the samples are kept at a constant temperature of 85 °C. A 405 nm laser at a repetition rate of 500 kHz (excitation density of ~3.4 x 10^{16} cm^{-3}) was used equipped with a 425 nm long-pass filter. The maps are recorded between 700 – 900 nm with a resolution of 1.5 nm. Before the measurement, the samples were illuminated for 10 min to account for halide segregation and the resulting red-shift of the PL peak. A high intensity is indicated by a yellow color, a low intensity is black. e)-h) Extracted lifetimes at the peak wavelength in each PL map for the e) I/Br, f) Rb-I/Br, g) Cs-I/Br, and h) RbCs-I/Br films. The lifetimes are shown for the initial map without temperature (black curves), during the temperature ramp of 2.3 °C /min (orange curves), and during the constant temperature of 85 °C (red curves).

To correlate the obtained optoelectronic changes to structural changes in the underlying perovskite structure, we perform in situ XRD measurements under light and elevated temperatures. Here, the films are placed on a metal ceramic heater and mounted into the XRD chamber. A white light source is used instead of a laser source to illuminate the whole sample area rather than a small spot. X-ray patterns were collected using a two-dimensional area detector, covering the angular range of 10 to 60°. The same heating profile as shown in the inset in Figure 2a is applied. Figures 4a-d show the obtained XRD maps as a function of time for all four samples. It can be seen that the perovskite-related reflections decrease in intensity

for the I/Br films whereas no changes in the intensity can be found for the cation-doped films. This decrease is consistent with perovskite decomposition, although the overall crystallographic texture of the perovskite is maintained. Figure 4e-h show a zoom in into the perovskite (100) reflection around 14° and the (110) as well as the (111) reflection in the range between 19° and 29°. We observe that an additional reflection grows in around 12.9° for the I/Br and Rb-I/Br samples, while no additional peak can be found for the Cs-I/Br and RbCs-I/Br samples. This additional reflection can be attributed to the formation of PbI_2. The reflection first appears when the sample temperature hits 85 C° for the I/Br sample. For Rb-I/Br the reflection starts to grow in after the sample temperature is kept at 85 C° for several minutes, indicating an improved stability.

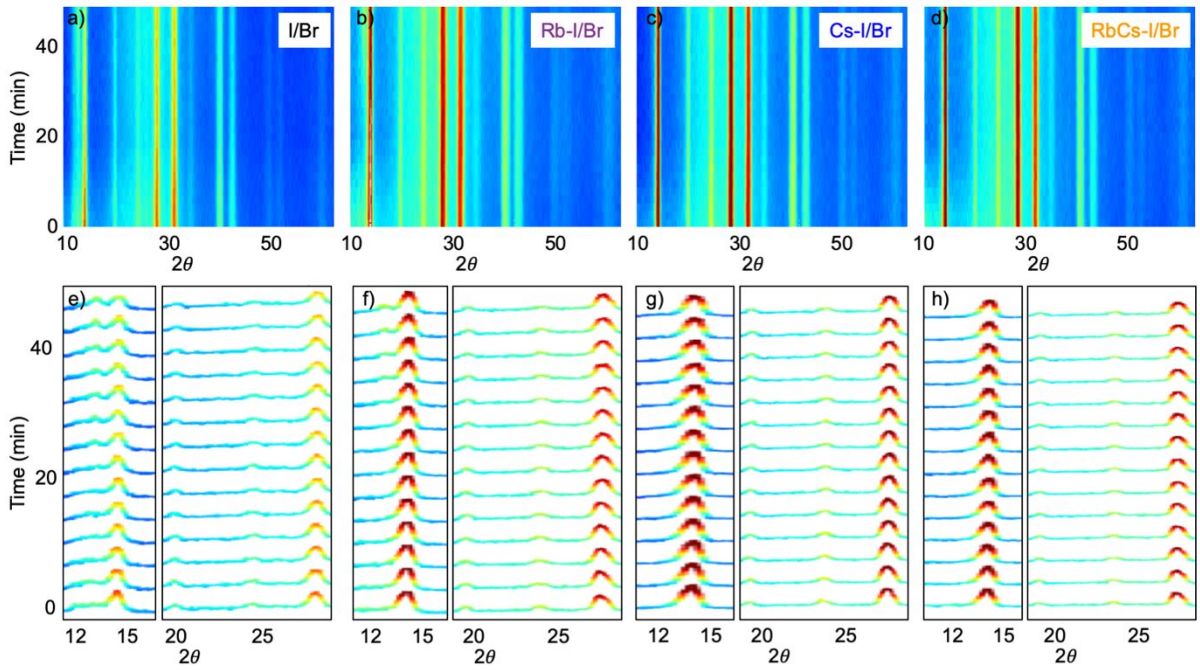

Figure 4. Light- and temperature-dependent XRD measurements for the a) I/Br, b) Rb-I/Br, c) Cs-I/Br, and d) RbCs-I/Br films. A white light source is used to study the influence of light and temperature on the structural characteristics of the films. The spectra are taken every 120 s. e)-h) Zoom in of the perovskite-related peak positions. An additional peak can be observed in the left panel for the e) I/Br, and f) Rb-I/Br, whereas no additional peak is seen for the g) Cs-I/Br, and h) RbCs-I/Br films. All peaks show a slight shift to higher angles when the temperature is increased toward 85 °C. The dashed lines indicate when the sample temperature hits the target temperature of 85 °C.

First, we will discuss the combined influence of light and temperature on the optical properties as seen in our experiments. As mentioned previously, the red-shift of the PL peak can be attributed to halide segregation resulting in local I-rich regions to reach the minimum Gibbs free energy under illumination, while the initially narrow PL peak can be attributed to charge carriers that have less thermal energy and thus, are located closer to the band edge.[28,49,50] It has also been reported that the induced strain can change the amount of phase segregation in different compositions or result in localized polarons.[51,52] By increasing the temperature, excess energy is provided into the system causing an increase in (hot) carriers which dissipate their energy by phonon emission. The resulting increase in electron-phonon coupling can lead to PL peak-broadening.[53,54] This excess energy also affects the driving force favoring halide segregation due to an imbalance between mixing entropy and specific energetics.[28] The increase in electron-phonon coupling has been also shown to accelerate the degradation of perovskite films, in particular the formation of PbI_2. The blue-shift of the PL especially at higher temperatures can be attributed to an increase in the degradation product PbI_2 which also manifests as an additional fast component in the PL decay dynamics.[55] Other explanations for such a blue-shift have been given by hot carrier relaxation and band edge state filling,[56] the Burstein-Moss effect[57,58] or a hot-phonon bottleneck.[57,59,60] For elevated temperatures, potential I_2 sublimation can also be considered. The quenching of the PL has been reported to depend on carrier localization and self-trapping due to the dynamic disorder of the perovskite lattice at elevated temperatures.[61]

However, to unravel the underlying mechanisms responsible for the changes in optoelectronic properties seen in our films, a structural method is required. Here, XRD is widely used as a figure of merit to support structural changes and phase transitions where temperature induces thermal expansion and potential phase transitions.[30,62,63] Phase transitions have been reported to lie within the operational range of PVs, for example, $MAPbI_3$ shows a phase transition at

55 °C, while mixed-cation compositions exhibit enhanced structural stability with phase transitions shifted to higher temperatures.[64] These structural changes could also be directly linked to an increase or decrease in performance of the films. Due to the ionic bonding character and dynamic crystal structure of the perovskite films,[65] thermal energy affects crystal lattice vibrations where activation energies of 42 meV have been reported for methyl groups.[66] The I-Pb-I bending mode is also coupled to the rotating dipoles of the methylammonium cations.[67] Further, under elevated temperatures thermal expansion effects occur in the perovskite lattice which are a function of the lattice parameters and temperature.[26] Additionally, it has been shown that in $MAPbI_3$ low-energy phonon modes are the main contributing factors for stabilizing the cubic phase at elevated temperatures.[68] Other studies have found a lower contribution for electron-phonon interactions in $MAPbI_3$.[69]

Besides temperature, structural changes due to light exposure have been studied by XRD where lattice strain contributes to an increase in electron-phonon interactions due to the polar coupling of optical phonons in the perovskite.[65] Longitudinal optical (LO) phonons have been found in halide perovskites, despite having only been previously reported in polar semiconductors such as GaAs.[53] The interaction between LO phonons and charge carriers have been shown to reduce charge carrier mobilities. Further, under optical illumination, strain is also greatly enhanced for phase segregated films due to the lattice mismatch between the different compositional regions within the film or by annihilation of halide vacancies and interstitials.[70] An increased distortion of the perovskite lattice during light illumination shifts the reflections to higher angles due to the dynamic perovskite crystal structure which can be attributed to a reduction in the unit cell volume.[27]

In our experiments, we have to carefully consider the influence of both stressors simultaneously, and we hypothesize that the underlying root cause for the decrease in performance of the perovskite films can be traced to the same origin. However depending on

the chemical stability of the perovskite films, we see a change in the crystal structure at elevated temperatures. For I/Br and Rb-I/Br, exposure to two stressors simultaneously results in rapid degradation, while an increased film stability and a non-rapid degradation is found for Cs-I/Br and RbCs-I/Br. Competing effects such as electronic- and structure-induced effects may be the underlying root cause for the observed degradation behavior. In the following, we will provide a detailed picture of the observed degradation behavior in which both effects are considered simultaneously.

Based on our experimental results, and as seen in Figure 4, the thermal stability of I/Br is the lowest of the systems studied, which also results in a strong decrease in optical performance. The reduction in the intensity of the X-ray reflections with increasing temperature indicates an increased thermal motion of the constituents. We estimate that the average mean square displacement increases by about 0.0001 $Å^2$, attenuating the observed intensity by about 10%. Thermal excitation tends to dynamically reduce the distortions of the perovskite lattice. Hence, the system becomes isotropic with an additional rotational degree of freedom of the sub-units and lifts the orientational degeneracy. We expect that this effect also has a major impact on phase separation and halide demixing based on the dynamic bonds forming the cubic perovskite lattice. An increase in entropy results in enhanced ion migration due to the lifting of the activation barrier which leads to the formation of the degradation product PbI_2. This is also shown experimentally in the I/Br film by the appearance of the reflection associated with formation of PbI_2 which indicates decomposition, and potentially, less of the MA/FA molecules. The addition of Rb increases the stability of the I/Br films resulting in stronger reflections at high angles and high temperatures. However, the addition of Rb does not eliminate the decomposition of the film and a similar degradation behavior can be seen as in the I/Br film, yet shifted to a later onset of degradation. On the other hand, an increase in stability and reduction in lattice strain is observed for RbCs-I/Br and Cs-I/Br, fully eliminating

the decomposition of the film over the course of the measurement. This is indicative that Cs is effective in stiffening the perovskite lattice, which can be attributed to a better size match for the $Pb(I,Br)_3$ sublattice as predicted by the Goldschmidt tolerance factor.

While we attribute the effect of light exposure and temperature to a difference in chemical stability resulting in a rapid vs. non-rapid degradation behavior for our films, in the following we will discuss how they impact the optoelectronic properties especially as seen previously in Figure 3 with regard to film (in)stability. In general, we observe an overall decrease in the PL and lifetime when the temperature hits 85 C° and is held for several minutes. This behavior can be explained by an increased interaction between phonons and charge carries. Here, the tilting of the octahedral frameworks at higher temperatures results in a strong electron-phonon coupling which is expected due to the polarizability of the ionic crystal lattice. Due to this large motion a pathway is created in which polarons can be formed, affecting the charge carrier recombination dynamics. By careful observation of the extracted lifetimes we find that an enhanced carrier lifetime coupled to a higher PL is obtained for the Cs-I/Br and RbCs-I/Br films at a temperature of approx. 50 - 60 C°. For I/Br and Rb-I/Br we find a decrease in carrier lifetimes upon reaching this temperature range. These effects could be explained by polaron formation as mentioned earlier which screen carriers leading to prolonged lifetimes for our Cs-doped perovskite thin films.[51,71] It has been suggested that the formation energy of polarons also depends on the rotation of the A-site molecules such as MA.[71] Thus, we hypothesize that based on the higher formation energy of polarons due to the higher disorder in our I/Br and Rb-I/Br films, a decrease in the lifetime is obtained compared to the Cs-doped films.

Lastly, we would like to mention that additional environmental factors such as oxygen and moisture could play a role in the observed PL behavior of our films.[72] For example, it has previously been reported that oxygen and humidity can lead to a photobrightening effect of the PL, since a superoxide species is formed which potentially passivates trap states.[73,74] In long-

time studies, it was also seen that oxygen and humidity can accelerate the degradation behavior.[75]

These results show that even if the perovskite films are not stable up to high temperatures, an increase in performance can be obtained under realistic PV operation conditions for various film compositions. Here, particularly the amount of stiffening of the lattice, and with it the changes in the phonon spectrum and the associated electron-phonon interactions can be tuned with the Rb/Cs ratio to find an optimal photoresponse of the system. It will be of future interest to study the reversibility of the observed behavior as well as to change the environmental conditions and study the effect of light and temperature under controlled atmospheres or for whole device architectures such as perovskite solar cells.

In conclusion, we studied the effect of Rb and Cs incorporation on the film stability based on I/Br ($(FA_{0.83}MA_{0.17})Pb(I_{0.83}Br_{0.17})_3$) when the perovskite films are exposed to light and elevated temperatures relevant to PV operations. While the Goldschmidt tolerance factor is used to assess whether a stable perovskite structure forms, the film stability under different stressors shows no correlation, rather it may be linked to the volatility of the A-site moieties. Our results reveal a rapid degradation for I/Br and Rb-I/Br films, while a non-rapid degradation was observed for Cs-I/Br and RbCs-I/Br films. The addition of Rb into the perovskite structure has only a marginal effect and shows similar film performances compared to the bare I/Br film when exposed to light and temperature. In particular, the decrease in optical response for the undoped I/Br and Rb-doped perovskite film can be traced to a combination of the degradation product $Pb(I/Br)_2$ and an enhanced electron-phonon coupling. Larger thermal motion was seen for the I/Br and Rb-I/Br films at higher temperatures and commensurate attenuation of the high angle reflections.

Contrary, for both Cs-doped films Cs-I/Br and RbCs-I/Br, we do not observe a decomposition of the perovskite at higher temperatures and light exposure. We attribute this to an increase in

chemical stability and that Cs is effective in stiffening the perovskite lattice, which can be attributed to a better size match for the $Pb(I,Br)_3$ sublattice as predicted by the Goldschmidt tolerance factor. These findings suggest that it is of importance to carefully select the stressors when assessing performance related parameters of PSCs.

EXPERIMENTAL METHODS

Perovskite film fabrication. Glass substrates were cleaned by sonication in a 2% Hellmanex solution, followed by deionized water and ethanol for 15 min each. The substrates were then placed in an UV ozone cleaner (Ossila) for 15 min. All perovskite films were prepared as reported previously.[42,44–46] Briefly, PbI_2 (TCI), $PbBr_2$ (TCI), MAI (Dyenamo), MABr (Dyenamo) and FAI (Dyenamo) were used as received. The perovskite solution was prepared using 1.1 M PbI_2, 1 M FAI, 0.22 M $PbBr_2$, and 0.2 M MABr in anhydrous DMF:DMSO (9:1, v:v). To add the additional cations, 1.5 M stock solutions of CsI (99.999% Sigma) in DMSO and RbI (99.9% Sigma) in DMF were added to the above solution in a 5:95 volume ratio. The perovskite films were then spin-coated in a two-step program: 1000 rpm for 10 s and 5000 rpm for 30 s. Chlorobenzene was used as antisolvent during the second spin-coating process. The films were annealed for 45 min at 100 °C. All experiments were carried out under ambient conditions without film encapsulation.

Optical characterization. The absorption properties of the films were measured using a UV-vis spectrometer (UV-2450, Shimadzu). The steady-state PL was measured using a OceanOptics spectrometer (HR2000+ES) under continuous excitation. A 405 nm (PicoQuant, LDH-D-C-405) laser diode was used as excitation source. To measure the film PL properties, PL spectra were recorded under continuous 405 nm excitation every 2 s for a total time of 45 min. To measure the influence of temperature on the PL properties, a metal ceramic heater (HT24S2, Thorlabs) was employed equipped with a 10 kΩ thermistor (TH10K, Thorlabs). The

ceramic heater was controlled by a temperature controller (TC 200, Thorlabs). The samples were heated to 85 °C using a ramp of 2.3 °C/min. After reaching the temperature of 85 °C, the samples were kept at this temperature for 20 min. Time-resolved PL lifetimes were measured via TCSPC using pulsed 405 nm excitation (PicoQuant, LDH-D-C-405) at an average power of 0.57 μW and a repetition rate of 61.25 kHz. Photon arrival times were detected by a single photon avalanche diode (MPD) and histogrammed by a HydraHarp 400 (Picoquant). The power of the incident laser beam was measured with a silicon power meter (PM100-D, Thorlabs).

Wavelength dependent maps were collected using a Gemini interferometer (NIREOS). The time resolution was set to 64 ps with a total of 65536 bins. The maps were recorded over 150 steps with a spectral range of 700 to 900 nm. Each step was integrated for 6001 ms. A picosecond pulsed laser diode (PicoQuant LDH-D-C-405) was used at a repetition frequency of 500 kHz to excite the films. Photon arrival times were collected via a silicon single-photon avalanche photodiode (Micro Photon Devices SPD-100-C0C) connected to a MultiHarp 150 (PicoQuant) event timer. A 425 nm long pass filter (ThorLabs) was used to removed excess laser scatter.

Topography measurements. The topography was measured using an AFM (Asylum MFP-3D) in tapping mode using a silicon cantilever.

XRD characterization.

The combined XRD studies using white light illumination, and temperature were carried out using a Bruker platform goniometer system with a 2D Vantec 500 area detector set up. The X-ray beam was aligned by a point focus collimator to assure a circular beam, rather than by a linear collimator. The circular 2D detector covers the angular range of 2θ from 10° to 65°. The range of the Psi angle (perpendicular to the 2θ axis) is not constant and depends on 2θ. The measured intensity function was integrated over the Psi axis. This integration over the Psi axis

and the circular beam averages out the different orientations of the sample. Thus, the presented results in Fig. 4 are independent of the sample orientation and its tilt angle. Each XRD pattern was recorded within 2 minutes, integrating over a temperature interval of 60 °C with a temperature ramp of 2.3 ºC/min. The 2-dimensional patterns were integrated using the Bruker EVA software suite. The Crystallography Open Database was used to characterize the integrated XRD spectra.[76]

ASSOCIATED CONTENT

Supporting Information

PL plots the four different film compositions, AFM topography images, PL plots without temperature and PL waterfall plots after heating the films.

AUTHOR INFORMATION

Current address

[#]Argonne National Laboratory, 9700 S. Cass Ave Lemont, IL 60439 USA

Corresponding Author

*Sarah Wieghold: swieghold@fsu.edu

*Lea Nienhaus: lnienhaus@fsu.edu

ORCID

Sarah Wieghold: 0000-0001-6169-3961

Lea Nienhaus: 0000-0003-1412-412X

Theo Siegrist: 0000-0001-5368-1442

Notes

The authors declare no competing financial interests.

ACKNOWLEDGEMENT

The authors gratefully acknowledge Florida State University startup funds. Part of the work was carried out at the National High Magnetic Field Laboratory, which is supported by the National Science Foundation under NSF DMR-1644779 and the State of Florida. We would like to thank Nick Bertone (PicoQuant) for the opportunity to demo the Gemini interferometer and Antonio Perri and Fabrizio Preda at NIREOS for their support with the Gemini.

REFERENCES

1 K. Galkowski, A. Mitioglu, A. Miyata, P. Plochocka, O. Portugall, G. E. Eperon, J. T.-W. Wang, T. Stergiopoulos, S. D. Stranks, H. J. Snaith and R. J. Nicholas, *Energy Environ. Sci.*, 2016, **9**, 962–970.
2 Y. Yang, M. Yang, Z. Li, R. Crisp, K. Zhu and M. C. Beard, *J. Phys. Chem. Lett.*, 2015, **6**, 4688–4692.
3 Y. Yamada, T. Nakamura, M. Endo, A. Wakamiya and Y. Kanemitsu, J. *Am. Chem. Soc.*, 2014, **163**, 11610-11613.
4 W. Tress, *Adv. Energy Mater.*, 2017, **7**, 1602358.
5 S. D. Stranks, G. E. Eperon, G. Grancini, C. Menelaou, M. J. P. Alcocer, T. Leijtens, L. M. Herz, A. Petrozza and H. J. Snaith, *Science*, 2013, **342**, 341.
6 G. Xing, N. Mathews, S. Sun, S. S. Lim, Y. M. Lam and M. Grätzel, *Science*, 2013, **342**, 344–347.
7 D. P. McKeekin, G. Sadoughi, W. Rehman, G. E. Eperon, M. Saliba, M. T. Hörantner, A. Haghighirad, N. Sakai, L. Korte, B. Rech, M. B. Johnston, L. M. Herz and H. J. Snaith, *Science*, 2016, **351**, 151–155.
8 C. Yi, J. Luo, S. Meloni, A. Boziki, N. Ashari-Astani, C. Grätzel, S. M. Zakeeruddin, U. Röthlisberger and M. Grätzel, *Energy Environ. Sci.*, 2016, **9**, 656–662.
9 N. J. Jeon, J. H. Noh, W. S. Yang, Y. C. Kim, S. Ryu, J. Seo and S. I. Seok, *Nature*, 2015, **517**, 476–480.
10 Q. Fu, X. Tang, B. Huang, T. Hu, L. Tan, L. Chen and Y. Chen, *Adv. Sci.*, 2018, **5**, 1700387.
11 N. Pellet, P. Gao, G. Gregori, T. Y. Yang, M. K. Nazeeruddin, J. Maier and M. Grätzel, *Angew. Chem. Int. Ed*, 2014, **53**, 3151–3157.
12 M. Saliba, T. Matsui, J. Seo, K. Domanski, J.-P. Correa-Baena, M. K. Nazeeruddin, S. M. Zakeeruddin, W. Tress, A. Abate, A. Hagfeldt and M. Grätzel, *Energy Environ. Sci.*, 2016, **9**, 1989–1997.
13 M. Saliba, T. Matsui, K. Domanski, J.-Y. Seo, A. Ummadisingu, S. M. Zakeeruddin, J.-P. Correa-Baena, W. R. Tress, A. Abate, A. Hagfeldt and M. Grätzel, *Science*, 2016, **354**, 206–209.
14 F. Li, Y. Pei, F. Xiao, T. Zeng, Z. Yang, J. Xu, J. Sun, B. Peng and M. Liu, *Nanoscale*, 2018, **10**, 6318–6322.
15 Y. Jiang, J. Yuan, Y. Ni, J. Yang, Y. Wang, T. Jiu, M. Yuan and J. Chen, *Joule*, 2018, **2**, 1356–1368.
16 T. Zhang, M. I. Dar, G. Li, F. Xu, N. Guo, M. Grätzel and Y. Zhao, *Sci Adv*, 2017, **3**, e1700841.
17 S.-H. Turren-Cruz, A. Hagfeldt and M. Saliba, *Science*, 2018, **362**, 449.

18 A. Solanki, P. Yadav, S.-H. Turren-Cruz, S. S. Lim, M. Saliba and T. C. Sum, *Nano Energy*, 2019, **58**, 604–611.

19 J. Tong, Z. Song, D. H. Kim, X. Chen, C. Chen, A. F. Palmstrom, P. F. Ndione, M. O. Reese, S. P. Dunfield, O. G. Reid, J. Liu, F. Zhang, S. P. Harvey, Z. Li, S. T. Christensen, G. Teeter, D. Zhao, M. M. Al-Jassim, M. F. A. M. van Hest, M. C. Beard, S. E. Shaheen, J. J. Berry, Y. Yan and K. Zhu, *Science*, 2019, **364**, 475.

20 S.-H. Turren-Cruz, M. Saliba, M. T. Mayer, H. Juarez-Santiesteban, X. Mathew, L. Nienhaus, W. Tress, M. P. Erodici, M.-J. Sher, M. G. Bawendi, M. Grätzel, A. Abate, A. Hagfeldt and J.-P. Correa-Baena, *Energy Environ. Sci.*, 2018, **11**, 78–86.

21 A. F. Gualdrón-Reyes, S. J. Yoon and I. Mora-Seró, *Current Opinion in Electrochemistry*, 2018, **11**, 84–90.

22 C. C. Boyd, R. Cheacharoen, T. Leijtens and M. D. McGehee, *Chem. Rev.*, 2019, **119**, 3418–3451.

23 K. Domanski, E. A. Alharbi, A. Hagfeldt, M. Grätzel and W. Tress, *Nature Energy*, 2018, **3**, 61–67.

24 Y. Hu, M. F. Aygüler, M. L. Petrus, T. Bein and P. Docampo, *ACS Energy Lett.*, 2017, **2**, 2212–2218.

25 Z. Song, A. Abate, S. C. Watthage, G. K. Liyanage, A. B. Phillips, U. Steiner, M. Graetzel and M. J. Heben, *Adv. Energy Mater.*, 2016, **6**, 1600846.

26 W. A. Saidi and A. Kachmar, *J. Phys. Chem. Lett.*, 2018, **9**, 7090–7097.

27 A. J. Barker, A. Sadhanala, F. Deschler, M. Gandini, S. P. Senanayak, P. M. Pearce, E. Mosconi, A. J. Pearson, Y. Wu, A. R. Srimath Kandada, T. Leijtens, F. De Angelis, S. E. Dutton, A. Petrozza and R. H. Friend, *ACS Energy Lett.*, 2017, **2**, 1416–1424.

28 M. C. Brennan, S. Draguta, P. V. Kamat and M. Kuno, *ACS Energy Lett.*, 2018, **3**, 204–213.

29 S. J. Yoon, M. Kuno and P. V. Kamat, *ACS Energy Lett.*, 2017, **2**, 1507–1514.

30 W. Tan, A. R. Bowring, A. C. Meng, M. D. McGehee and P. C. McIntyre, *ACS Appl. Mater. Interfaces*, 2018, **10**, 5485–5491.

31 J. Yang, X. Liu, Y. Zhang, X. Zheng, X. He, H. Wang, F. Yue, S. Braun, J. Chen, J. Xu, Y. Li, Y. Jin, J. Tang, C. Duan, M. Fahlman and Q. Bao, *Nano Energy*, 2018, **54**, 218–226.

32 W. Tress, K. Domanski, B. Carlsen, A. Agarwalla, E. A. Alharbi, M. Graetzel and A. Hagfeldt, *Nature Energy*, 2019, **4**, 568–574.

33 M. V. Khenkin, E. A. Katz, A. Abate, G. Bardizza, J. J. Berry, C. Brabec, F. Brunetti, V. Bulović, Q. Burlingame, A. Di Carlo, R. Cheacharoen, Y.-B. Cheng, A. Colsmann, S. Cros, K. Domanski, M. Dusza, C. J. Fell, S. R. Forrest, Y. Galagan, D. Di Girolamo, M. Grätzel, A. Hagfeldt, E. von Hauff, H. Hoppe, J. Kettle, H. Köbler, M. S. Leite, S. (Frank) Liu, Y.-L. Loo, J. M. Luther, C.-Q. Ma, M. Madsen, M. Manceau, M. Matheron, M. McGehee, R. Meitzner, M. K. Nazeeruddin, A. F. Nogueira, Ç. Odabaşı, A. Osherov, N.-G. Park, M. O. Reese, F. De Rossi, M. Saliba, U. S. Schubert, H. J. Snaith, S. D. Stranks, W. Tress, P. A. Troshin, V. Turkovic, S. Veenstra, I. Visoly-Fisher, A. Walsh, T. Watson, H. Xie, R. Yıldırım, S. M. Zakeeruddin, K. Zhu and M. Lira-Cantu, *Nature Energy*, 2020, **5**, 35–49.

34 M. A. Jensen, A. E. Morishige, S. Chakraborty, R. Sharma, H. S. Laine, B. Lai, V. Rose, A. Youssef, E. E. Looney, S. Wieghold, J. R. Poindexter, J. Correa-Baena, T. Felisca, H. Savin, J. B. Li and T. Buonassisi, *IEEE Journal of Photovoltaics*, 2018, **8**, 448–455.

35 M. A. Jensen, A. Zuschlag, S. Wieghold, D. Skorka, A. E. Morishige, G. Hahn and T. Buonassisi, *Journal of Applied Physics*, 2018, **124**, 085701.

36 F. Kersten, P. Engelhart, H.-C. Ploigt, A. Stekolnikov, T. Lindner, F. Stenzel, M. Bartzsch, A. Szpeth, K. Petter, J. Heitmann and J. W. Müller, *Solar Energy Materials and Solar Cells*, 2015, **142**, 83–86.

37 J.-P. Correa-Baena, M. Saliba, T. Buonassisi, M. Grätzel, A. Abate, W. Tress and A. Hagfeldt, *Science*, 2017, **358**, 739–744.

38 G. Grancini and M. K. Nazeeruddin, *Nature Reviews Materials*, 2019, **4**, 4–22.
39 J.-P. Correa-Baena, Y. Luo, T. M. Brenner, J. Snaider, S. Sun, X. Li, M. A. Jensen, N. T. P. Hartono, L. Nienhaus, S. Wieghold, J. R. Poindexter, S. Wang, Y. S. Meng, T. Wang, B. Lai, M. V. Holt, Z. Cai, M. G. Bawendi, L. Huang, T. Buonassisi and D. P. Fenning, *Science*, 2019, **363**, 627–631.
40 G. Kieslich, S. Sun and A. K. Cheetham, *Chem. Sci.*, 2014, **5**, 4712–4715.
41 T. Duong, H. K. Mulmudi, H. Shen, Y. Wu, C. Barugkin, Y. O. Mayon, H. T. Nguyen, D. Macdonald, J. Peng, M. Lockrey, W. Li, Y.-B. Cheng, T. P. White, K. Weber and K. Catchpole, *Nano Energy*, 2016, **30**, 330–340.
42 S. Wieghold, J. Tresback, J.-P. Correa-Baena, N. T. P. Hartono, S. Sun, Z. Liu, M. Layurova, Z. A. VanOrman, A. S. Bieber, J. Thapa, B. Lai, Z. Cai, L. Nienhaus and T. Buonassisi, *Chem. Mater.*, 2019, **31**, 3712–3721.
43 T. J. Jacobsson, J.-P. Correa-Baena, E. H. Anaraki, B. Philippe, S. D. Stranks, M. E. F. Bouduban, W. Tress, K. Schenk, J. Teuscher, J.-E. Moser, H. Rensmo and A. Hagfeldt, *J. Am. Chem. Soc.*, 2016, **138**, 10331–10343.
44 J.-P. Correa-Baena, Y. Luo, T. M. Brenner, J. Snaider, S. Sun, X. Li, M. A. Jensen, N. T. P. Hartono, L. Nienhaus, S. Wieghold, J. R. Poindexter, S. Wang, Y. S. Meng, T. Wang, B. Lai, M. V. Holt, Z. Cai, M. G. Bawendi, L. Huang, T. Buonassisi and D. P. Fenning, *Science*, 2019, **363**, 627.
45 S. Wieghold, J.-P. Correa-Baena, L. Nienhaus, S. Sun, K. E. Shulenberger, Z. Liu, J. S. Tresback, S. S. Shin, M. G. Bawendi and T. Buonassisi, *ACS Appl. Energy Mater.*, 2018, **1**, 6801–6808.
46 S. Wieghold, J. Correa-Baena, L. Nienhaus, S. Sun, J. S. Tresback, Z. Liu, S. S. Shin, M. G. Bawendi and T. Buonassisi, in *2018 IEEE 7th World Conference on Photovoltaic Energy Conversion (WCPEC) (A Joint Conference of 45th IEEE PVSC, 28th PVSEC & 34th EU PVSEC)*, 2018, pp. 2553–2556.
47 E. T. Hoke, D. J. Slotcavage, E. R. Dohner, A. R. Bowring, H. I. Karunadasa and M. D. McGehee, *Chem. Sci.*, 2015, **6**, 613–617.
48 S. S. Lim, D. Giovanni, Q. Zhang, A. Solanki, N. F. Jamaludin, J. W. M. Lim, N. Mathews, S. Mhaisalkar, M. S. Pshenichnikov and T. C. Sum, *Sci Adv*, 2019, **5**, eaax3620.
49 C. Barugkin, J. Cong, T. Duong, S. Rahman, H. T. Nguyen, D. Macdonald, T. P. White and K. R. Catchpole, *J. Phys. Chem. Lett.*, 2015, **6**, 767–772.
50 R. E. Beal, N. Z. Hagström, J. Barrier, A. Gold-Parker, R. Prasanna, K. A. Bush, D. Passarello, L. T. Schelhas, K. Brüning, C. J. Tassone, H.-G. Steinrück, M. D. McGehee, M. F. Toney and A. F. Nogueira, *Matter*, 2020, **2**, 207–219.
51 C. G. Bischak, C. L. Hetherington, H. Wu, S. Aloni, D. F. Ogletree, D. T. Limmer and N. S. Ginsberg, *Nano Lett.*, 2017, **17**, 1028–1033.
52 C. M. Sutter-Fella, Q. P. Ngo, N. Cefarin, K. L. Gardner, N. Tamura, C. V. Stan, W. S. Drisdell, A. Javey, F. M. Toma and I. D. Sharp, *Nano Lett.*, 2018, **18**, 3473–3480.
53 A. D. Wright, C. Verdi, R. L. Milot, G. E. Eperon, M. A. Pérez-Osorio, H. J. Snaith, F. Giustino, M. B. Johnston and L. M. Herz, *Nature Commun.*, 2016, **7**, 11755.
54 J.-Y. Yang and M. Hu, *J. Phys. Chem. Lett.*, 2017, **8**, 3720–3725.
55 A. Merdasa, A. Kiligaridis, C. Rehermann, M. Abdi-Jalebi, J. Stöber, B. Louis, M. Gerhard, S. D. Stranks, E. L. Unger and I. G. Scheblykin, *ACS Energy Lett.*, 2019, **4**, 1370–1378.
56 H.-H. Fang, S. Adjokatse, S. Shao, J. Even and M. A. Loi, *Nature Commun.*, 2018, **9**, 243.
57 M. B. Price, J. Butkus, T. C. Jellicoe, A. Sadhanala, A. Briane, J. E. Halpert, K. Broch, J. M. Hodgkiss, R. H. Friend and F. Deschler, *Nature Commun.*, 2015, **6**, 8420.
58 J. Fu, Q. Xu, G. Han, B. Wu, C. H. A. Huan, M. L. Leek and T. C. Sum, *Nature Commun.*, 2017, **8**, 1300.

59 Y. Yang, D. P. Ostrowski, R. M. France, K. Zhu, J. van de Lagemaat, J. M. Luther and M. C. Beard, *Nature Photonics*, 2016, **10**, 53–59.

60 H. Zhu, K. Miyata, Y. Fu, J. Wang, P. P. Joshi, D. Niesner, K. W. Williams, S. Jin and X.-Y. Zhu, *Science*, 2016, **353**, 1409.

61 K. T. Munson, E. R. Kennehan, G. S. Doucette and J. B. Asbury, *Chem*, 2018, **4**, 2826–2843.

62 T. J. Jacobsson, L. J. Schwan, M. Ottosson, A. Hagfeldt and T. Edvinsson, *Inorg. Chem.*, 2015, **54**, 10678–10685.

63 T. Meier, T. P. Gujar, A. Schönleber, S. Olthof, K. Meerholz, S. van Smaalen, F. Panzer, M. Thelakkat and A. Köhler, *J. Mater. Chem. C*, 2018, **6**, 7512–7519.

64 H. Zheng, J. Dai, J. Duan, F. Chen, G. Zhu, F. Wang and C. Xu, *J. Mater. Chem. C*, 2017, **5**, 12057–12061.

65 D. T. Limmer and N. S. Ginsberg, *arXiv*, 2020, 2001.01677.

66 J. Li, M. Bouchard, P. Reiss, D. Aldakov, S. Pouget, R. Demadrille, C. Aumaitre, B. Frick, D. Djurado, M. Rossi and P. Rinke, *J. Phys. Chem. Lett.*, 2018, **9**, 3969–3977.

67 B. Kang and K. Biswas, *J. Phys. Chem. C*, 2017, **121**, 8319–8326.

68 W. A. Saidi and J. J. Choi, *J. Chem. Phys.*, 2016, **145**, 144702.

69 A. Francisco-López, B. Charles, O. J. Weber, M. I. Alonso, M. Garriga, M. Campoy-Quiles, M. T. Weller and A. R. Goñi, *J. Phys. Chem. Lett.*, 2019, **10**, 2971–2977.

70 E. Mosconi, D. Meggiolaro, H. J. Snaith, S. D. Stranks and F. De Angelis, *Energy Environ. Sci.*, 2016, **9**, 3180–3187.

71 F. Zheng and L. Wang, *Energy Environ. Sci.*, 2019, **12**, 1219–1230.

72 A. J. Knight, A. D. Wright, J. B. Patel, D. P. McMeekin, H. J. Snaith, M. B. Johnston and L. M. Herz, *ACS Energy Lett.*, 2019, **4**, 75–84.

73 R. Brenes, C. Eames, V. Bulović, M. S. Islam and S. D. Stranks, *Advanced Materials*, 2018, **30**, 1706208.

74 X. Feng, H. Su, Y. Wu, H. Wu, J. Xie, X. Liu, J. Fan, J. Dai and Z. He, *J. Mater. Chem. A*, 2017, **5**, 12048–12053.

75 N. Aristidou, I. Sanchez-Molina, T. Chotchuangchutchaval, M. Brown, L. Martinez, T. Rath and S. A. Haque, *Angewandte Chemie International Edition*, 2015, **54**, 8208–8212.

76 S. Gražulis, D. Chateigner, R. T. Downs, A. F. T. Yokochi, M. Quirós, L. Lutterotti, E. Manakova, J. Butkus, P. Moeck and A. Le Bail, *J Appl Crystallogr*, 2009, **42**, 726–729.